3D Multibody-Discrete Element Co-Simulations of Flexible Wheel Performance for Small Planetary Rovers

Cristiano Pizzamiglio*
Department of Mechanical and Aerospace Engineering
Politecnico di Torino
Turin, Italy
cristiano.pizzamiglio@polito.it

Giancarlo Genta
Department of Mechanical and Aerospace Engineering
Politecnico di Torino
Turin, Italy
giancarlo.genta@polito.it

Alessandra Cofano
International Research School of Planetary Sciences
Università d'Annunzio
Pescara, Italy
cofano@irsps.unich.it

Abstract

The aim of this paper is to assess the tractive performance of flexible wheels for lightweight planetary rovers using a multibody-discrete element method (DEM) co-simulation framework. By reducing the pressure exerted on the ground, flexible wheels may experience lower sinkage and reduced compaction resistance. Two different discrete element models of the tested soil were implemented using two and four-sphere particles. The bulk calibration approach was used to identify the values of particle-particle static friction coefficient, shear modulus and packing density of the bulk material. A single wheel test rig was designed and built to compare the experimental data to the DEM results and the results obtained with a semi-empirical model based on the classical terramechanics theories. Regarding the drawbar pull, the two discrete element models showed good agreement with the experimental results, especially at low slips (0.0÷0.2). The semi-empirical model performed well at low slips but a discrepancy is evident at higher slips (0.4÷0.6). The discrete element models gave better approximation of the sinkage, with respect to the classical model, in particular at slips ranging from 0.4 to 0.6. The co-simulations required a relevant computational cost.

1 Introduction

The serious mobility issues encountered by the Mars Exploration Rovers (MERs) have led researches, e.g. Johnson et al. (2015), to the development of numerical frameworks that can overcome the limitations of

*Corresponding author and project principal investigator.

the classical terramechanics models. For instance, the latter do not take into account soil inhomogeneities and soil profile (Smith et al., 2013), and provide less accurate results for vehicles having wheels with a diameter smaller than 50 cm (Bekker, 1969). Despite these limitations, it is important to bear in mind the historical importance of these widely used semi-empirical models that, thanks to their computational efficiency, can be employed to design, optimize and simulate tracked and wheeled vehicles (Wong, 2010).

In contrast to the previous approach, the discrete element method offers the possibility of accurately modelling the micromechanics of granular materials, i.e. allows to study soils at particle-scale level taking into account their shape, size, kinematics and forces exchanged among them and with solid geometries. From the collective interactions of the particles, the bulk behavior of the soil emerges. Hence, DEM algorithms are suitable for simulating scenarios that involve terrain inhomogeneities, high sinkage and high slip ratios (Smith et al., 2013; Johnson et al., 2015). However, those benefits come with a major drawback recognized by many authors, i.e. the high computational effort required to run DEM simulations, thus making problematic the modelling of large-scale applications that may involve millions of discrete elements.

Some of the successful applications of the discrete element method for analyzing the performance of the locomotion subsystem of planetary rovers are briefly summarized. Smith et al. (2013) modelled the steady-state interaction between a 130 mm radius rigid wheel and a soil modelled as a collection of single sphere particles having a uniform distribution ranging from 2.5 to 10 mm; DEM parameters were calibrated using the bulk calibration approach (see Section 5), namely by simulating direct shear and pressure-sinkage tests; single wheel tests carried out using the discrete element method provided results closer to experimental measurements with respect to the classical and dynamic Bekker methods but with a high computational cost. Discrete element analyses of drawbar pull and sinkage of Mars Exploration Rover wheel were performed by Johnson et al. (2015) using mono-dispersed tri-sphere particles with a circumscribed sphere radius of 3.9 mm; the outcomes of the numerical tests matched accurately the laboratory results for slips equal to 0.5 and 0.7, while for low slips the accuracy of the predictions increased for higher values of both interparticle friction coefficient and packing density of the DEM soil bed. Knuth et al. (2012) developed three-dimensional DEM simulations to study the MER wheel interaction with the martian regolith and to analyze the regolith deformation in a geotechnical triaxial strength cell; in particular, sinkage and torque values obtained from the wheel digging simulation using poly-ellipsoid particles were in good agreement with the experimental data. For modelling the wheel flexibility, Nishiyama et al. (2016) developed a two-dimensional simulation framework that combines both finite and discrete element methods, obtaining tractive performance predictions for planetary rovers similar to the experimental values.

This paper is structured as follows. In the next section, a model for a driving flexible wheel is developed based on the classical terramechanics theories. In Section 3 the discrete element algorithm implemented in the EDEM software is discussed in detailed, followed by Section 4 which describes the properties of the martian soil simulant used for the laboratory tests. Section 5 addresses the calibration of the DEM parameters focusing on the selection of the particle shape. Section 6 is devoted to the setup of the single wheel experimental and DEM tests, and to the development of the multibody model of the wheel that takes into account its elasticity. In Section 7 the results obtained from the semi-empirical method and the discrete element simulations are analyzed and compared to the experimental measurements. Finally, the Section *Conclusion and future works* shows how the multibody-discrete element co-simulations are currently used for designing flexible wheels and analyzing their performance.

2 Semi-empirical model for flexible wheels

Based on the fundamental works by Bekker (1956, 1960, 1969), Wong and Reece (1967a,b) and Wong (1984), semi-empirical methods are extensively used to predict and optimize the performance of tracked and off-road wheeled vehicles for terrestrial and extraterrestrial applications.

A wheel is considered flexible when the average ground pressure p_g exerted on hard ground is less than the

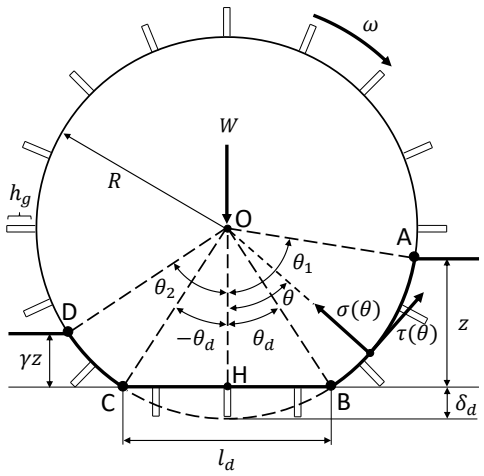

Parameter	Definition	Unit
k_c	Cohesive modulus of deformation	$\mathrm{N/m^{m+1}}$
k_ϕ	Friction modulus of deformation	$\mathrm{N/m^{m+2}}$
n	Sinkage exponent	-
R	Wheel radius	m
b	Wheel width	m
b_s	Smallest dimension of contact area	m
W	Vertical load	N
θ_1, θ_2	Entry/exit contact angles	rad
θ_d	Deflection angle	rad
l_d	Length section $\overline{BC}$	m
δ_d	Wheel vertical deformation	m
γ	Exit angle coefficient	-
z	Wheel sinkage	m
ω	Wheel angular velocity	$\mathrm{rad\,s^{-1}}$
h_b	Grouser height	m

Figure 1: Flexible wheel-soil interaction model.

critical ground pressure p_{gcr} given by the following equation (Wong, 1978):

$$p_{gcr} = \left[\frac{k_c}{b_s} + k_\phi\right]^{\frac{1}{2n+1}} \left[\frac{3W}{(3-n)b\sqrt{2R}}\right]^{\frac{2n}{2n+1}}, \tag{1}$$

where the meaning of the parameters is reported in Figure 1. The average ground pressure of the wheel under examination was evaluated via a MSC Nastran implicit nonlinear finite element analysis (SOL400).

In the pneumatic tire model developed by Wong (2010) and in the model by Ishigami et al. (2011) for flexible wheels for planetary rovers, the deflected area of the wheel is assumed to be flat and the front and rear sections of the contact interface are considered circular. Instead, Favaedi et al. (2011) proposed to approximate the front and rear sections of the ExoMars wheel as elliptical arcs. Shmulevich and Osetinsky (2003) suggested a parabolic profile for the deformed section of a pneumatic tire. In this model, the Wong approach was selected, therefore the deflected area is flat and the front and rear sections of the contact patch are circular as shown in Figure 1. Moreover, the normal stress distribution is considered to be uniform.

The length L_{BC} of the flat contact section $\overline{BC}$ and the deflection angle θ_d (angle $\angle HOB$ between the vertical segment $\overline{OH}$ and segment $\overline{OB}$) are expressed as:

$$L_{BC} = 2\sqrt{2R\delta_d - \delta_d^2}, \qquad \theta_d = \arccos\left(1 - \frac{\delta_d}{R}\right),$$

where δ_d is the wheel vertical deformation and is computed with a discrete element analysis (see Section 6.2), whilst Favaedi et al. (2011) modelled the wheel on three-dimensional terrain profiles using the finite element method. The entry contact angle θ_1 and the exit contact angle θ_2 can be written in the following way:

$$\theta_1 = \arccos\left(\cos\theta_d - \frac{z}{R}\right), \qquad \theta_2 = \arccos\left(\cos\theta_d - \frac{\gamma z}{R}\right),$$

where z is the wheel sinkage and γ is the exit angle coefficient.

The normal stress distribution $\sigma(\theta)$ for a driving wheel on soft soil in the three contact sections was modelled using both the pressure-sinkage relation developed by Bekker (1960)

$$p = \left(\frac{k_c}{b_s} + k_\phi\right) z^n = k_{eq} z^n,$$

and the approach proposed by Ishigami et al. (2011), who developed a model for both flexible and rigid wheels for exploration rovers:

$$\sigma(\theta) = \begin{cases} \sigma_{AB}(\theta) = k_{eq} R^n \left(\cos\theta - \cos\theta_1\right)^n & \text{if } \theta_d \leq \theta \leq \theta_1, \\ \sigma_{BC}(\theta) = k_{eq} R^n \left(\cos\theta_d - \cos\theta_1\right)^n & \text{if } -\theta_d \leq \theta < \theta_d, \\ \sigma_{CD}(\theta) = k_{eq} R^n \left[\cos\left(\theta_1 - \dfrac{\theta - \theta_2}{\theta_m - \theta_2}\left(\theta_1 - \theta_m\right)\right) - \cos\theta_1\right]^n & \text{if } \theta_2 \leq \theta < -\theta_d. \end{cases} \tag{2}$$

The expression of the angle θ_m at which the normal stress is maximum is given by (Wong and Reece, 1967a):

$$\theta_m = \left(c_1 + c_2 s\right)\theta_1$$

where the value of the coefficients c_1 and c_2 depends on soil conditions (Wong, 2010) - usually $c_1 \approx 0.4$ and c_2 ranges from 0.0 to 0.3 (Ishigami et al., 2011). As pointed out by Ishigami et al. (2011), if θ_m is greater than θ_d the third stress equation of the System 2 has to be solved for $\theta_2 \leq \theta < -\theta_d$ and $\theta_d \leq \theta < \theta_m$. The slip ratio s for a driving wheel is defined below:

$$s = 1 - \frac{v}{R\omega} \quad \text{if } |R\omega| \geq |v|.$$

The shear stress distribution $\tau(\theta)$ at the contact interface is derived by the Janosi and Hanamoto (1961) empirical formulation which includes the Mohr-Coulomb failure criterion:

$$\tau(\theta) = \left[c + \sigma(\theta)\tan\phi\right]\left(1 - e^{-\frac{j(\theta)}{K}}\right)$$

where c, ϕ and K denote the cohesion, angle of internal friction and shear deformation modulus of the soil respectively. The soil shear displacement j along section $\widehat{AB}$ is computed as

$$j_{AB}(\theta) = R\left[\theta_1 - \theta - (1-s)\left(\sin\theta_1 - \sin\theta\right)\right],$$

whereas along the deflected section $\overline{BC}$ is equal to:

$$\begin{aligned} j_{BC}(\theta) &= j_{AB}(\theta_d) + j_d \\ &= j_{AB}(\theta_d) + \int_{\theta}^{\theta_d} Rs\cos\theta\, d\theta \\ &= r\left[\theta_1 - \theta_d - (1-s)\left(\sin\theta_1 - \sin\theta_d\right) + s\left(\sin\theta_d - \sin\theta\right)\right]; \end{aligned}$$

similarly the expression for the soil shear displacement along section $\widehat{CD}$ can be derived as:

$$j_{CD}(\theta) = j_{BC}(-\theta_d) + \int_{\theta}^{-\theta_d} R\left[1 - (1-s)\cos\theta\right]\, d\theta.$$

The knowledge of the normal and shear stress distributions along the wheel-soil contact interface allows to write the equation of force equilibrium in the vertical z direction:

$$W = F_z = bR\int_{\theta_d}^{\theta_1}\left[\sigma_{AB}(\theta)\cos\theta + \tau_{AB}(\theta)\sin\theta\right]\, d\theta + bl_d\sigma_{BC} + bR\int_{\theta_2}^{-\theta_d}\left[\sigma_{CD}(\theta)\cos\theta + \tau_{CD}(\theta)\sin\theta\right]\, d\theta. \tag{3}$$

The entry and exit angles for the various slip ratios were evaluated following the iterative process proposed by Ishigami et al. (2011). The value of the sinkage in static condition was chosen as initial guess for the sinkage z of the wheel in the dynamic state. The latter allowed to compute θ_1 and θ_2 and, therefore, to solve Equation 3. The value of the sinkage z was increased until the condition

$$|W - F_z| < err$$

was met, where *err* is the maximum error permitted. The static sinkage was computed by solving for θ_{1s} the nonlinear equation below:

$$0 = -W + 2bk_{eq}R^{n+1}\int_{\theta_d}^{\theta_{1s}} \left[\cos(x) - cos(\theta_{1s})\right]^n \, d\theta + bl_d\sigma_{BC}.$$

The drawbar pull DP is obtained by computing the difference between total thrust and compaction resistance. The total thrust H generated by the wheel is given by the sum of the thrust contributions in the three contact sections:

$$\begin{aligned} H(s) &= H_{AB}(s) + H_{BC}(s) + H_{CD}(s) \\ &= bR\left(\int_{\theta_d}^{\theta_1} \tau_{AB}(\theta)\cos\theta\, d\theta + \int_{-\theta_d}^{\theta_d} \tau_{BC}(\theta)\cos\theta\, d\theta + \int_{\theta_2}^{-\theta_d} \tau_{CD}(\theta)\cos\theta\, d\theta\right). \end{aligned}$$

To take into account the grouser contribution to the overall thrust, a fourth term has to be added to the previous equation. The thrust generated by the grousers was modelled using the approach developed by Bekker (1956) and adopted by Favaedi et al. (2011):

$$F_g = b\left(\frac{1}{2}\gamma_s h_g^2 N_\phi + q h_g N_\phi + 2c h_g \sqrt{N_\phi}\right),$$

where q is the surcharge, γ_s denotes the soil weight density and N_ϕ is defined as:

$$N_\phi = \tan^2\left(45^\circ + \frac{\phi}{2}\right).$$

The total resistance force RF is due to soil compaction at the front section $\widehat{AB}$ and rear section $\widehat{CD}$ and to wheel flexing resistance R_f (experimentally determined):

$$\begin{aligned} RF &= RF_{AB} + RF_{CD} + R_f \\ &= bR\left(\int_{\theta_d}^{\theta_1} \sigma_{AB}(\theta)\sin\theta\, d\theta + \int_{\theta_2}^{-\theta_d} \sigma_{CD}(\theta)\sin\theta\, d\theta\right) + R_f. \end{aligned}$$

Lastly, the resistance torque is given by:

$$\begin{aligned} T(s) &= T_{AB}(s) + T_{BC}(s) + T_{CD}(s) \\ &= bR^2\left(\int_{\theta_d}^{\theta_1} \tau_{AB}(\theta)\, d\theta + \int_{\theta_d}^{\theta_1} \tau_{BC}(\theta)\, d\theta + \int_{\theta_d}^{\theta_1} \tau_{CD}(\theta)\, d\theta\right). \end{aligned}$$

The code was implemented in MATLAB R2017a. Since pressure-sinkage parameters were unknown, their values were taken from the literature by selecting a soil having physical properties as similar as possible to the soil used for this project (Ishigami et al., 2011), namely $n = 1.0$, $k_c = 1.37 \times 10^3\,\mathrm{N/m^{n+1}}$ and $k_\phi = 8.14 \times 10^5\,\mathrm{N/m^{n+2}}$. Setting c_1 to 0.1 and c_2 to 0.2 allowed to get results closer to the experimental data.

3 The discrete element method

The discrete element method (DEM), also known as distinct element method, is a particle-scale numerical method for modelling the bulk behavior of granular materials. The method was first applied by Cundall and Strack (1979) for the analysis of geomechanics problems. Currently the DEM is used in a wide range of applications ranging from agricultural to pharmaceutical ones. The remarkable increase of papers published (Figure 2) highlights the growing interest of the scientific community towards DEM and its ability to

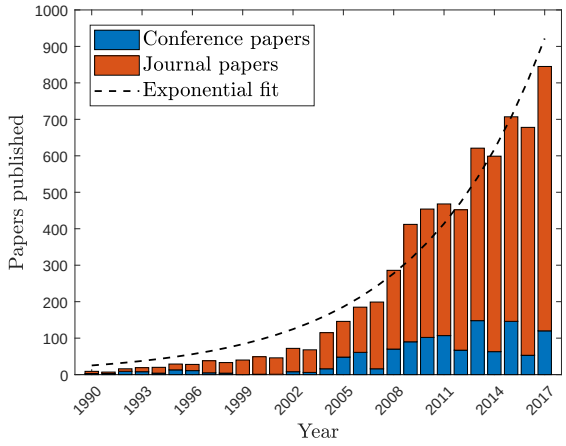

Figure 2: Journal and conference papers published from 1990 to 2017 in the DEM field. The analysis was performed on the Scopus database by using the following keywords in the title and abstract: "discrete element method/model", "distinct element method/model", "discrete element simulations".

accurately analyze discontinuous and granular flows of matter. The bibliometric analysis in Figure 2 was performed using the approach of O'Sullivan (2014).

The soil used in the experimental tests was modelled using the EDEM software developed by the company DEM Solutions Ltd. EDEM allows to implement clumps of spherical particles; non-spherical particles are not supported yet. All the DEM simulations were performed using the Hertz-Mindlin contact model. The normal force F_n is a function of the normal overlap δ_n and is given by

$$F_n = \frac{4}{3} E_{eq} \sqrt{R_{eq}} \delta_n^{3/2}$$

where the equivalent Young's modulus E_{eq} is calculated as

$$\frac{1}{E_{eq}} = \frac{(1-\nu_i^2)}{E_i} + \frac{(1-\nu_j^2)}{E_j}$$

and the equivalent radius R_{eq} can be written as

$$\frac{1}{R_{eq}} = \frac{1}{R_i} + \frac{1}{R_j}$$

The quantities E_i, ν_i, R_i and E_j, ν_j, R_j are the Young's modulus, Poisson ratio and radius respectively of each sphere in contact. The tangential force F_t depends on the tangential overlap δ_t and is modelled as

$$F_t = -S_t \delta_t$$

where S_t is the tangential stiffness and is given by

$$S_t = 8 G_{eq} \sqrt{R_{eq} \delta_n}$$

and G_{eq} is the equivalent shear modulus.
The damping component of the normal force can be calculated as

$$F_n^d = -2\sqrt{\frac{5}{6}} \beta \sqrt{S_n m_{eq}} v_n^{rel}$$

where m_{eq} is the equivalent mass defined as

$$m_{eq} = \left(\frac{1}{m_i} + \frac{1}{m_j} \right)^{-1}$$

v_n^{rel} is the normal component of the relative velocity and S_n is the normal stiffness given by the following equation

$$S_n = 2E_{eq}\sqrt{R_{eq}\delta_n}$$

The damping coefficient β is related to the coefficient of restitution as described by Tsuji et al. (1992) and can be written as

$$\beta = \frac{\ln e}{\sqrt{\ln^2 e + \pi^2}}$$

Regarding the damping component of the tangential force, it can be computed as

$$F_t^d = -2\sqrt{\frac{5}{6}}\beta\sqrt{S_t m_{eq}}v_t^{rel}$$

where v_t^{rel} is the relative tangential velocity. The tangential force is limited by Coulomb friction μF_n where μ is the static friction coefficient.

An efficient grid-based search algorithm is utilized for contact detection and its workflow can be summarized as follows (EDEM, 2017b):

1. The simulation domain is subdivided into three-dimensional cubic cells. Cell size depends on the application, particle size distribution, the dynamics of the system and other factors.
2. Active cells (those containing two or more particles) are identified.
3. Contacts between particles are detected by measuring the distances between neighboring particles.
4. Forces and moments acting on the elements are computed.
5. The position of the elements is updated.
6. The active cells are updated and the process is repeated.

All the simulations were run setting the grid cell size equal to three times the smallest sphere radius in the model.

For an exhaustive explanation of DEM theory, the authors suggest to read Cundall and Strack (1979), Zhang and Whiten (1996) and Matuttis and Chen (2014).

Table 1: Physical properties of the tested soil.

Parameter	Value	Unit
Cohesion	≈ 0	kPa
Angle of internal friction	42.6	deg
Young's modulus	21.8	MPa
Poisson ratio	0.25	-
Particle density	2659	$\mathrm{kg\,m^{-3}}$
Angle of repose	31.6	deg

4 Mars soil simulant

The soil tested was provided by the Italian company Altec S.p.A. and its physical properties (listed in Table 1) were investigated at the International Research School of Planetary Sciences (Pescara, Italy).

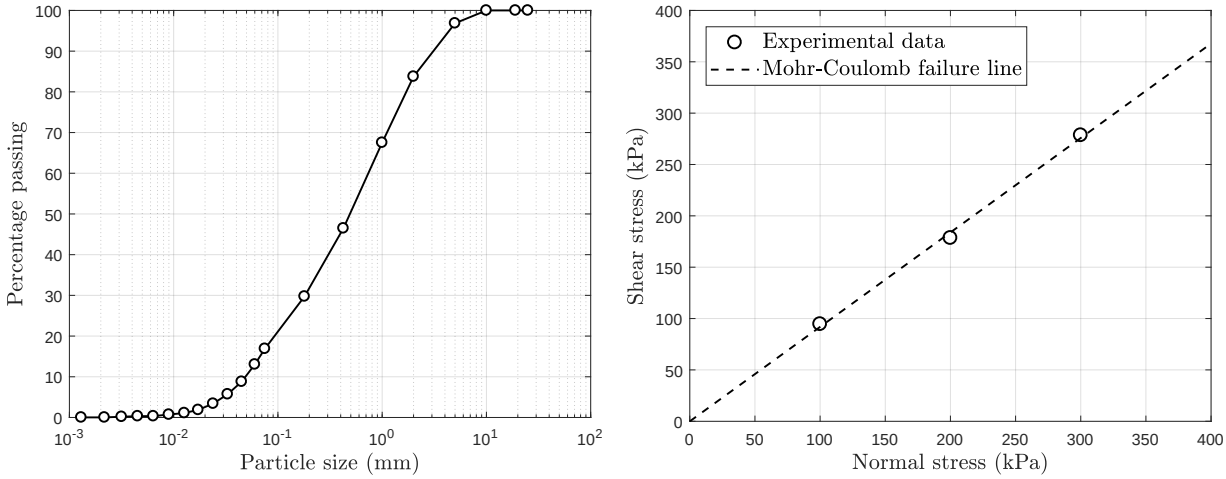

Figure 3: **Left**: Grain size distribution. The gravel (>2 mm) and sand (0.06 ÷ 2 mm) fractions are 16% and 74% respectively; the clay/silt component (0.002 ÷ 0.06 mm) is equal to 10%. **Right**: Mohr-Coulomb failure line obtained from direct shear tests. Tests were carried out at three different normal pressures: 100, 200 and 300 kPa.

The particle size distribution in Figure 3 left reveals that the soil simulant is a gravelly sand with a small silt fraction. The effective size of the distribution, D_{10}, is equal to 0.05 mm and the uniformity coefficient C_u, given by the ratio of D_{60} to D_{10}, is 14.8 indicating a well graded soil.

Direct shear tests and consolidated and drained triaxial tests were conducted to evaluate cohesion, angle of internal friction and the modulus of elasticity, whereas the pycnometer test was performed to estimate the particle density. The Mohr-Coulomb failure line obtained by processing the direct shear test results and illustrated in Figure 3 right shows the cohesionless nature of the soil and an angle of internal friction equal to 42.6°.

5 Calibration of DEM parameters

Reproducing the bulk behavior of a granular material modelled as an assemblage of discrete particles requires the accurate estimation of a set of micro-scale input parameters: particle size, shape, Young's modulus, Poisson ratio and density; coefficients of static/rolling friction and coefficient of restitution between particles and between particles and geometries. As pointed out by many researchers (for instance Briend et al., 2011; Derakhshani et al., 2015), the calibration of DEM parameters is a demanding and essential task to perform, however there is a lack of a standardized calibration procedure (Coetzee, 2017). Marigo and Stitt (2015) identified two calibration methods commonly adopted in literature that are briefly described below:

- Direct measurement of the input parameter values from experimental tests. The major drawback of this approach is that some mechanical properties such as the Poisson ratio or the coefficient of restitution can be challenging to determine.
- Discrete element simulations of bulk experiments (e.g. direct shear tests, triaxial shear tests). DEM input parameters are iteratively changed until the numerical model shows a macroscopic behavior comparable with the measured bulk response. Pizette et al. (2010) and Marigo and Stitt (2015) highlight a criticality of this approach, i.e. more than one set of input parameter values may generate a similar macroscopic response. Moreover, as emphasized by Coetzee (2017), the DEM parameters calibrated for a specific model are not necessarily the optimum values for another model. Coetzee (2017) refers to this approach as *bulk calibration approach*.

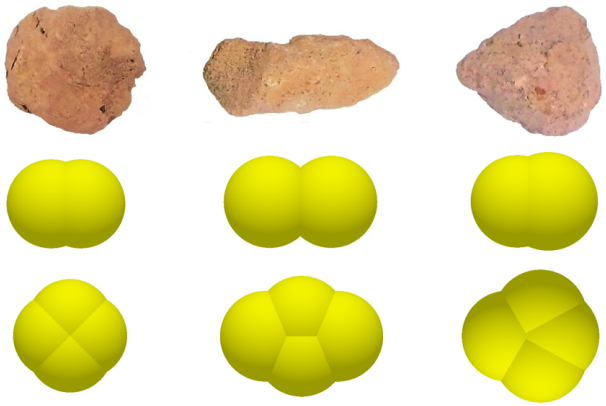

Figure 4: DEM particle shapes. The first row shows a picture of the grains randomly taken from the soil sample. The second and third rows display two-sphere and four-sphere models of the real soil grains respectively.

The second calibration method was chosen for this study and the direct shear and the angle of repose tests were simulated to find the best set of DEM parameters. With the aim of reducing the computational effort and the total number of virtual tests, restitution coefficients and the coefficient of static friction between particles and walls were taken from the literature. The calibrated values are listed in Table 2.

5.1 Particle size and shape

The selection of the discrete element size and shape was greatly affected by the computational resources available for this study. The simulations were run on a machine equipped with an Intel® Core$^{(TM)}$ i7-4510U CPU (2.0 GHz, two cores, four threads). In the EDEM software, the time step is defined as a percentage of the Rayleigh time step, T_R, which is the time taken for a shear wave to propagate through a solid particle, calculated as (EDEM, 2017b):

$$T_R = \left(\frac{\rho}{G}\right)^{\frac{1}{2}} \frac{\pi r}{0.1631\nu + 0.8766}, \tag{4}$$

where r is the smallest sphere radius in the simulation, ρ is the particle density, G is the shear modulus and ν the Poisson ratio. As indicated by Equation 4, the Rayleigh time step is proportional to the sphere radius, thus implementing in the DEM model the real granular distribution would result in a very high number of elements and in an excessively low time step. Hence, the so-called *particle scaling technique* (Marigo and Stitt, 2015) was adopted and a nominal sphere radius equal to 3.0 mm was selected as a good trade-off between hardware resources and accuracy of simulation results. In addition, the sphere radius distribution randomly varies from 0.9 to 1.1 times the nominal size.

Element shape significantly affect the bulk behavior of the granular material. For instance, spherical particles may be unsuitable to reproduce the interlocking phenomenon (González-Montellano et al., 2011; Johnson et al., 2015) or bulk friction similar to the tested material (Coetzee, 2016). The DEM simulations were carried out using clumps consisting of two or four spheres and, for each clump type, three different sphere arrangements were defined by analyzing the shapes of the grains of size bigger than 2 mm (Figure 4). Since clumps of spheres were implemented, the coefficient of rolling friction was not considered in the parameter tuning process as, for example, Coetzee (2016) did. All the DEM simulations were run with the three particle shapes distributed in equal parts.

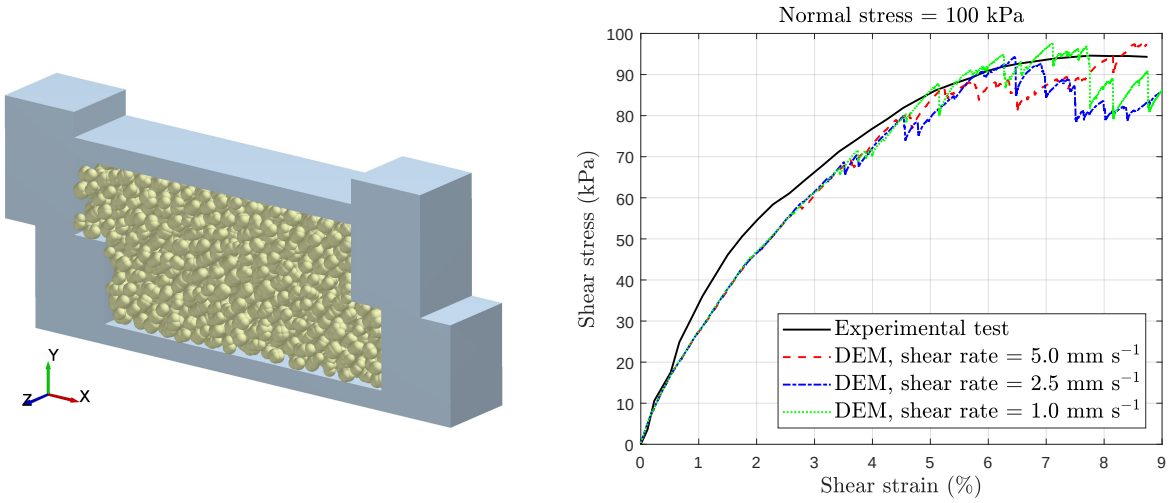

Figure 5: **Left**: Discrete element simulation of a direct shear test using 4-sphere clump subjected to a normal stress equal to 100 kPa. The static friction coefficient and the particle stiffness were set to 0.9 and 5.0×10^7 Pa respectively. **Right**: Comparison between experimental data and DEM results with varying shear rate.

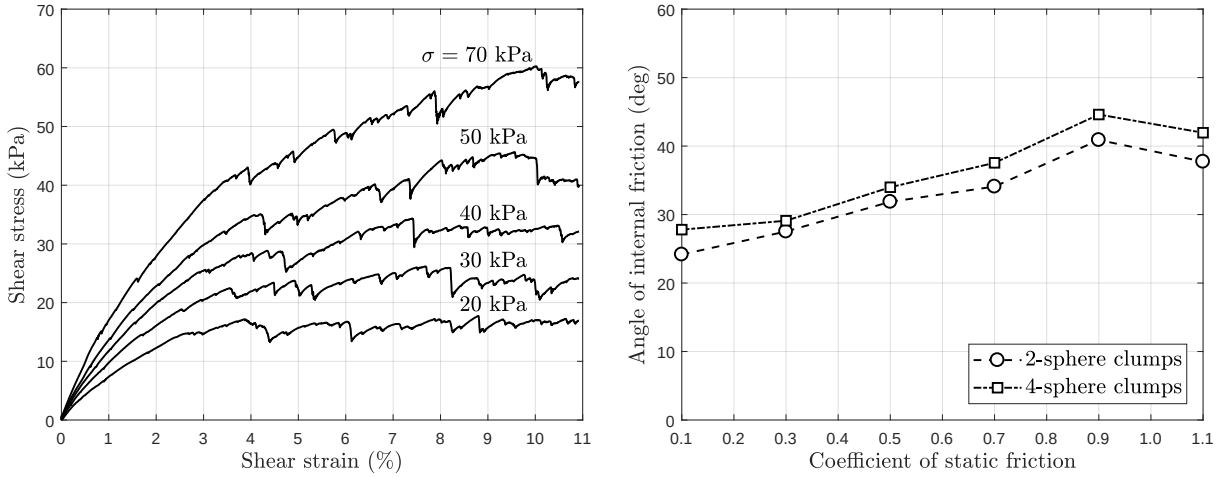

Figure 6: **Left**: Shear stress-strain curves for two-sphere clumps. **Right**: The material angles of internal friction, measured from the simulations with two and four-sphere clumps, as a function of the static friction coefficient.

5.2 Static friction coefficient and shear modulus

More than 220 virtual direct shear tests were performed to identify the values for the coefficient of static friction and shear modulus of the bulk material for the two and four-sphere clumps that better approximate the experimental value of both cohesion and angle of internal friction of the tested regolith simulant.

In literature the direct shear test was modelled in different ways. Ucgul et al. (2015) implemented a 200 mm long, 100 mm wide and 100 mm deep virtual shear box with the lower box translating at a constant shear rate of 0.02 mm s^{-1}; the normal stresses were set to 15.3, 51.6 and 103 kPa. A shear box of approximately 10×8×1.5 mm consisting of 1865 spherical particles was modelled by Briend (2010); periodic boundaries were employed to reduce the number of particles and the shearing process was simulated for 0.45 s by moving

Table 2: Calibrated parameters for the two-sphere and four-sphere clumps. Sphere density was slightly increased with respect to the experimental value in order to increase the simulation time step.

Parameter	2-sphere clumps	4-sphere clumps	Unit	Source
Particle-wall restitution coeff., e_w	0.5		-	EDEM database
Particle-particle restitution coeff., e	0.5		-	Briend (2010)
Particle-wall friction coeff., μ_w	0.5		-	Ucgul et al. (2015)
Particle-particle friction coeff., μ	0.9	0.9	-	Virtual tests
Wall Poisson's ratio, ν_w	0.29		-	EDEM databse
Soil Poisson's ratio, ν	0.25		-	Experimental test
Wall shear modulus, G_w	8.023×10^{10}		Pa	EDEM databse
Soil shear modulus, G	2×10^7	3×10^7	Pa	Virtual tests
Wall density, ρ_w	7800		$\mathrm{kg\,m^{-3}}$	EDEM databse
Sphere density, ρ	2759		$\mathrm{kg\,m^{-3}}$	Experimental test
Sphere size distribution	0.9 - 1.1		-	Virtual tests
Cohesion, c	0.47	0.19	kPa	Virtual tests
Angle of internal friction, ϕ	40.89	44.61	deg	Virtual tests
Angle of repose, A	29.67	30.31	deg	Virtual tests

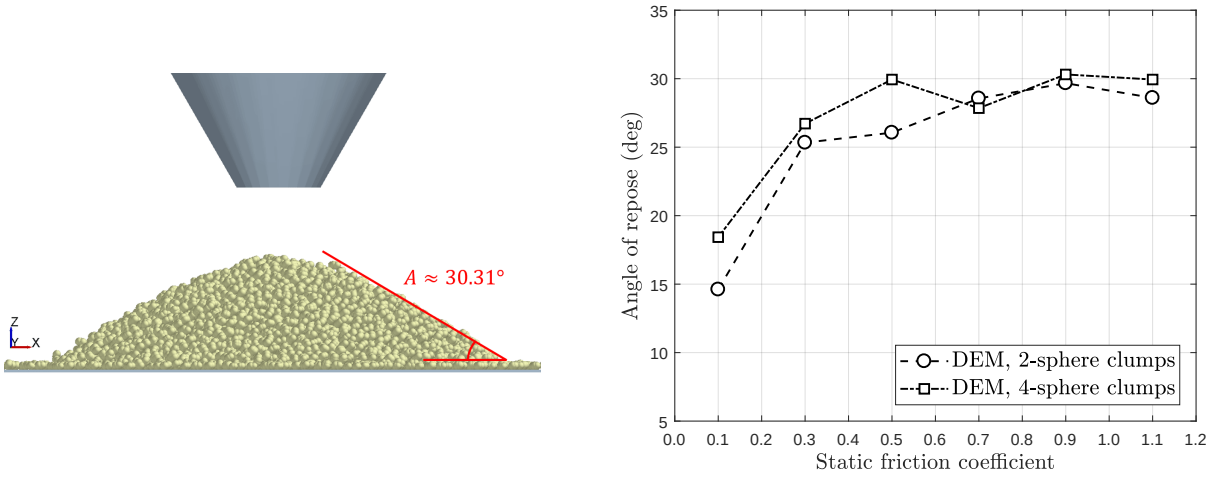

Figure 7: **Left**: Discrete element simulation of the angle of repose test using four-sphere clumps. The particle-particle static friction coefficient is equal to 0.9. **Right**: Angle of repose as a function of the static friction coefficient. The DEM results from two and four-sphere clumps simulations are compared.

the lower box at $3\,\mathrm{mm\,s^{-1}}$; normal loads of 50, 75, 100 and 150 kPa were applied on the spheres through a massless rectangular particle. The overall dimensions of the shear box created by Smith et al. (2013) are $60\times60\times60$ mm and the normal pressure (2.08, 5.33 and 17.83 kPa) was imposed with a plate made of tightly packed particles grouped into a rigid body; in this case the upper frame was moved at a constant speed of $0.66\,\mathrm{mm\,s^{-1}}$ for a distance of 6.6 mm.

For this project, a shear box of $160\times80\times40$ mm, containing approximately 1580 clumps, with periodic boundaries in the z-direction was modelled. After a 0.4 s consolidation phase, the shear process was simulated by moving the lower frame at a constant shear rate of $5\,\mathrm{mm\,s^{-1}}$ for 3.5 s. By dividing the soil reaction force on the lower frame with the corrected area of the sheared section, the shear stress was computed. Normal stresses of 20, 30, 40, 50 and 70 kPa were selected according to the normal loads acting on the granular material during the actual applications. Indeed, the DEM model of the soil was developed for testing not

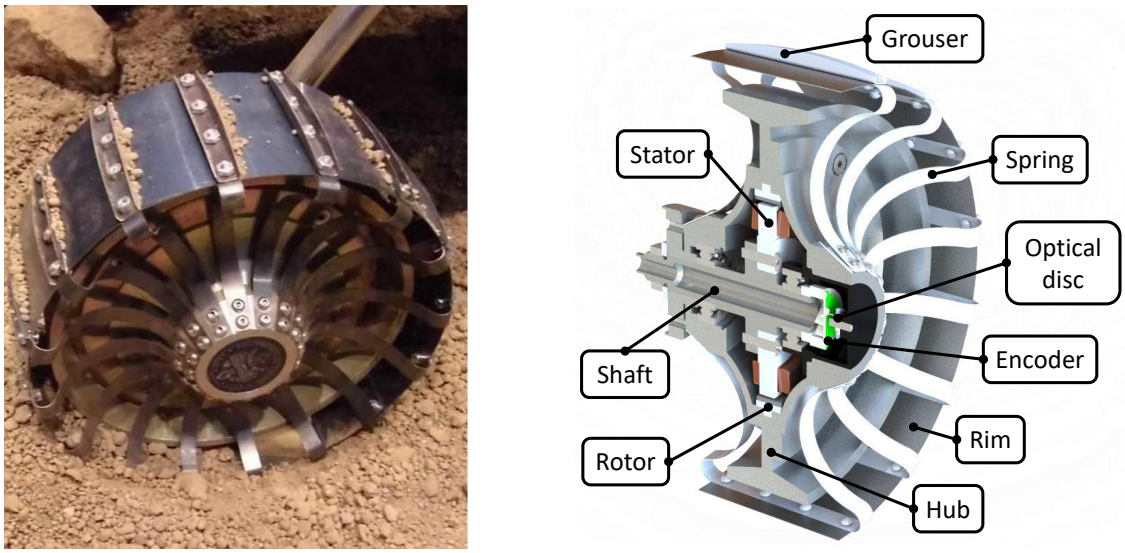

Figure 8: **Left**: The tested flexible wheel made of spring steel. **Right**: CAD rendering of the cross-section of the AMALIA wheel. The hub contains a brushless DC motor with external rotor. A 10 mm hollow shaft allows the motor electrical cables to enter the inner part of the wheel.

only the performance of the flexible wheels, but also of rigid wheels and legged vehicles. The maximum shear stresses were plotted as a function of the corresponding normal stresses to evaluate cohesion and angle of internal friction. The void ratio e was set as close as possible to the experimental value of about 1.0, i.e. 0.78 and 0.89 for the two and four-sphere clumps respectively. In Figure 5 left, a numerical direct shear test with the four-sphere clumps is depicted during the shearing phase with a normal pressure equal to 100 kPa and Figure 5 right displays the very good agreement between experimental data and DEM results. Moreover, Figure 5 right shows that the shear stress-strain curve is not affected by the shear rate, as confirmed by Smith et al. (2013), allowing to choose a higher speed for the lower frame, hence reducing the simulation time. The shear stress-strain curves for two-sphere clumps and different vertical loads are plotted in Figure 6 left, whereas Figure 6 right highlights the nonlinearity of the angle of internal friction as a function of the coefficient of static friction for the two clump types. The wall time taken by a virtual direct shear test with four-sphere clumps and shear modulus of the bulk material set to 2×10^7 Pa is about 78 minutes.

The angle of repose tests were numerically replicated by filling a funnel with approximately 8880 clumps (Figure 7 left) and the numerical results for the two and four-sphere clumps as a function of the coefficient of static friction are reported in Figure 7 right. This test turned out to be not particularly useful since the angle of repose tends to assume an asymptotic value for static friction coefficient values ranging from 0.5 to 1.1, making not possible the selection of a particular value for the friction coefficient; the same consideration was also proven by Coetzee (2016). It can be also noticed from Figure 7 right that with the four-sphere clumps the angle of repose is on average slightly higher with respect to the two-sphere clumps; the relative error between the experimental value of the angle of repose and the two and four-sphere clump simulations are 6.11% and 4.08% respectively. The wall time taken by a DEM simulation of the angle of repose test with four-sphere clumps is about 154 minutes.

6 AMALIA wheel testing

Experimental and numerical single wheel tests at constant and positive slip ratios were performed on the flexible wheel (Figure 8) of the AMALIA engineering model of a lightweight planetary rover designed and built by the space robotics group Team DIANA at Politecnico di Torino for the Google Lunar XPRIZE competition. The AMALIA rover is a 30 kg four-wheeled vehicle that features in-wheel hub brushless DC

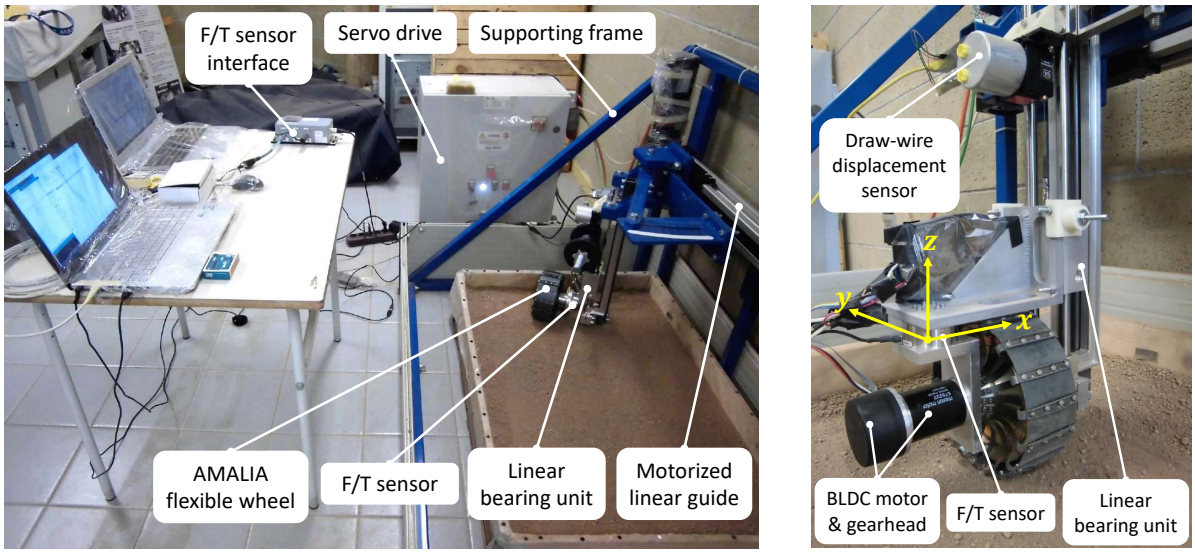

Figure 9: **Left**: Overview of the singe wheel test bench. **Right**: The AMALIA wheel connected to the suspension unit. In this picture the load cell reference frame is depicted in yellow.

motor and an active suspension system for pitch and roll control. The latter system is a longitudinal swing arm suspension actuated by a servomotor and coupled to a two-stage spur gear reduction. The suspensions act as legs to cross obstacles whose height would be not manageable by a conventional passive suspension (Genta and Marenco, 2014). The flexible wheel is made of spring steel (AISI 304) and its diameter and width are 180 mm and 70 mm respectively. The 16 pairs of springs constituting the sides of the wheel are 27.5 mm radius circular beams clamped at the hub and attached to the rim through a 5 mm radius arc. The springs are arranged in a configuration similar to the reinforcement wires of the sides of a radial tire, whereas the rim is arranged in the same way as the reinforcement of the belt plys. Both rim and springs are made of a 0.4 mm thick sheet metal.

6.1 Experimental setup

The single wheel test rig developed can be employed for testing both towed (Figure 9, left) and powered wheels (Figure 9, right). The overall test bench dimensions are 2730 mm in length, 1090 mm in width and 1040 mm in height, and the maximum soil depth is 280 mm. A motorized toothed-belt driven linear guide with a 2000 mm stroke transmits the longitudinal motion to the wheel and is supported by a steel tube frame which allows the guide to be positioned at different heights to compensate for wheel diameter and soil depth. The wheel can translate in the vertical direction thanks to a linear bearing unit that slides along two 16 mm diameter precision steel shafts. The latter are fixed to the linear guide by means of stiffening beams which also bear torsional and flexural loads generated by the wheel-soil interaction. The steering angle can be manually set up to 25° but it cannot be changed during the test. The normal load is imposed through cast-iron weights supported by an aluminum structure connected to the linear bearing unit. The in-wheel hub custom motor was removed and a 100 W brushless DC Maxon EC 60 flat motor, having nominal torque of 0.227 N m and coupled to a planetary gearhead with 66:1 reduction, provides torque to the wheel; the motor is controlled by a VESC controller[1], i.e. an open source speed controller having CAN-bus or USB interface and provided with a STM32F4 microcontroller. A six-axis force/torque ATI FT Mini45 sensor with IP65 protection placed between the motor support and the linear bearing unit measures drawbar pull, normal load and side force. The vertical displacement of the wheel hub was monitored with a Micro-Epsilon draw-wire displacement sensor.

[1] http://vedder.se/2015/01/vesc-open-source-esc/

Table 3: Experimental single wheel test parameters

Parameter	Value	Unit
Soil bin dimensions (L×W×D)	1155×760×130	mm
Wheel diameter	180	mm
Rim width	70	mm
Grouser height	7	mm
Wheel angular velocity	2.73	rpm
Normal load	42.1, 61.7	N
Slip ratio	0.0, 0.1, 0.2, 0.3, 0.4, 0.5, 0.6	-
Travelling distance	700	mm

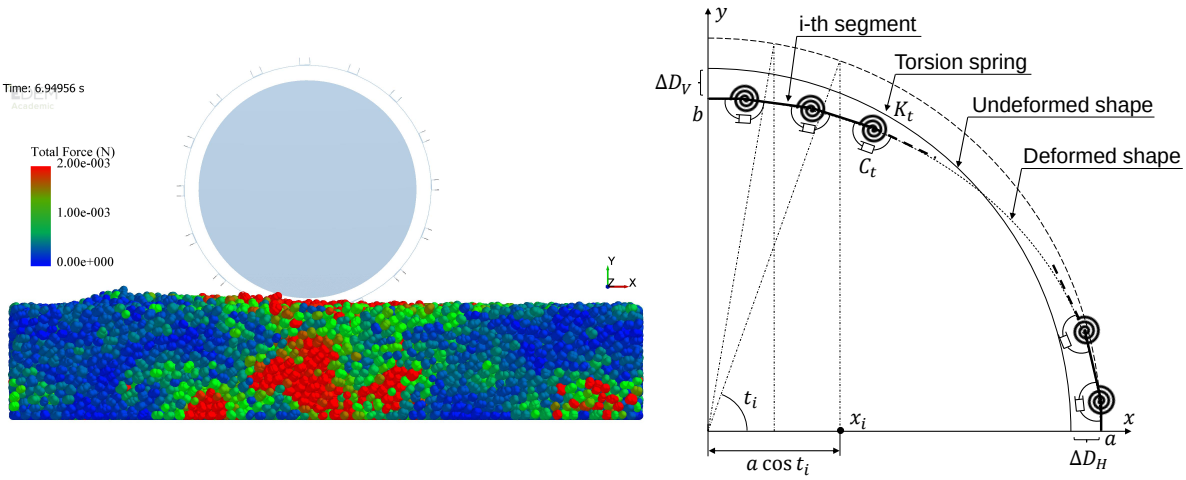

Figure 10: **Left**: Multibody-discrete element method co-simulation of the AMALIA wheel ($s = 0.4$). The image also shows the particle contact forces. **Right**: Diagram of the lumped parameter model of the flexible wheel.

By keeping the AMALIA wheel angular velocity fixed at 2.73 rpm and varying the linear guide speed, different slip ratios can be set. For each test, the wheel travelling distance was selected equal to 700 mm, the slip ratio ranged from 0.0 to 0.6 with a 0.1 step and the steering angle was set to zero degrees. Tests were repeated for two normal loads (42.1 N and 61.7 N). Given the small wheel diameter, the soil bin length, width and depth were reduced to 1155 mm, 760 mm and 130 mm respectively. The experimental test parameters are summarized in Table 3.

6.2 Multibody-discrete element co-simulations

In this section the setup of the flexible wheel co-simulations is addressed. First the creation of the DEM particle bed is described, afterwards the development of the multibody dynamics model (MBD) of the AMALIA wheel in the Adams software environment is discussed.

A 480 mm-long, 220 mm-wide and 100 mm-deep soil bed was created with periodic boundaries in the x and z directions to limit the number of particles, hence speeding up the numerical tests (Figure 10 left). Under the influence of Earth gravity, particles rained down, from the static factory[2] used to generate them, thus filling the soil bed. During this process the coefficient of static friction was modified to achieve different

[2]Particle factories are used to define where, when and how particles appear in a simulation. A static factory produces particles at a specified time (EDEM, 2017a).

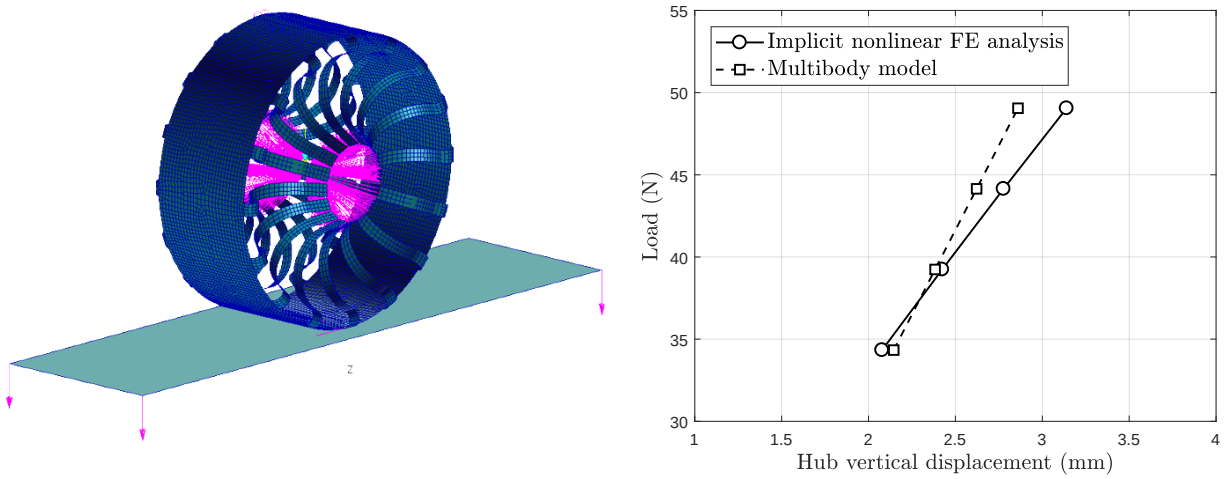

Figure 11: **Left**: Finite element model of the AMALIA wheel developed with the Patran pre/post-processor; the finite element nonlinear static analysis (SOL400) with contact was performed using the Nastran solver. **Right**: Comparison between the finite element model and the multibody model of the wheel.

packing density (PD) values; a PD equal to 0.57 and 0.52 for the two and four-sphere clumps respectively minimized the relative error between laboratory and DEM tests. As highlighted by Das (2007) and Zhu et al. (2008), PD plays an important role in shear force generation in cohensionless soil; to further prove this statement, Johnson et al. (2015) and Smith et al. (2013) took into account the PD for the discrete element simulations of the wheel performance of planetary rovers. In particular, Johnson et al. (2015) created a DEM particle bed with constant, specified PD as a function of depth. After the particles settled into the bin, the particle friction coefficient was restored to its calibrated value. From $t = 0.0\,\mathrm{s}$ to $t = 0.1\,\mathrm{s}$ the wheel gets in contact with the soil surface and from $t = 0.1\,\mathrm{s}$ to $t = 0.2\,\mathrm{s}$ the wheel angular and linear speeds reach their experimental values; the simulation time ranged from 7 to 10 s depending on the slip ratio. The co-simulation were run considering a vertical load of 42.1 N acting on the wheel. The wall time taken by a 10 s single-wheel test with four-sphere clumps is approximately equal to 624 minutes and a total of 72 co-simulations were run.

The wheel flexibility was reproduced by substituting the circular beams with translational spring-dampers and by discretizing the rim with a number of segments, i.e. rigid bodies connected by revolute joints and rotational spring-dampers (Figure 10 right). The stiffness of the latter was computed using the following approximate method based on the Castigliano's second theorem. Let us consider a circular ring with the same dimensions of the actual wheel rim subjected to a vertical load W. In the case of deformation smaller than 15% of the rim diameter, the shape of the deformed ring can be reasonably approximated to elliptical. The changes in the vertical and horizontal diameters of the circular ring can be calculated using the following equations (Young and Budynas, 2002):

$$\Delta D_H = 0.1366\frac{WR^3}{EI}, \qquad \Delta D_V = -0.1488\frac{WR^3}{EI},$$

where R is the ring radius, E is the spring steel modulus of elasticity and I is area moment of inertia of the ring cross section about the principal axis perpendicular to the plane of the ring. Therefore, the length of the semi-major and semi-minor axis of the ellipse can be respectively computed as:

$$a = R + \Delta D_H/2, \qquad b = R + \Delta D_V/2.$$

It can be proved that for a thin circular ring, the expression of the total elastic energy U stored in the structure under load is given by

$$U = \frac{W^2R^3}{EI}\left(\frac{\pi}{16} - \frac{1}{2\pi}\right), \tag{5}$$

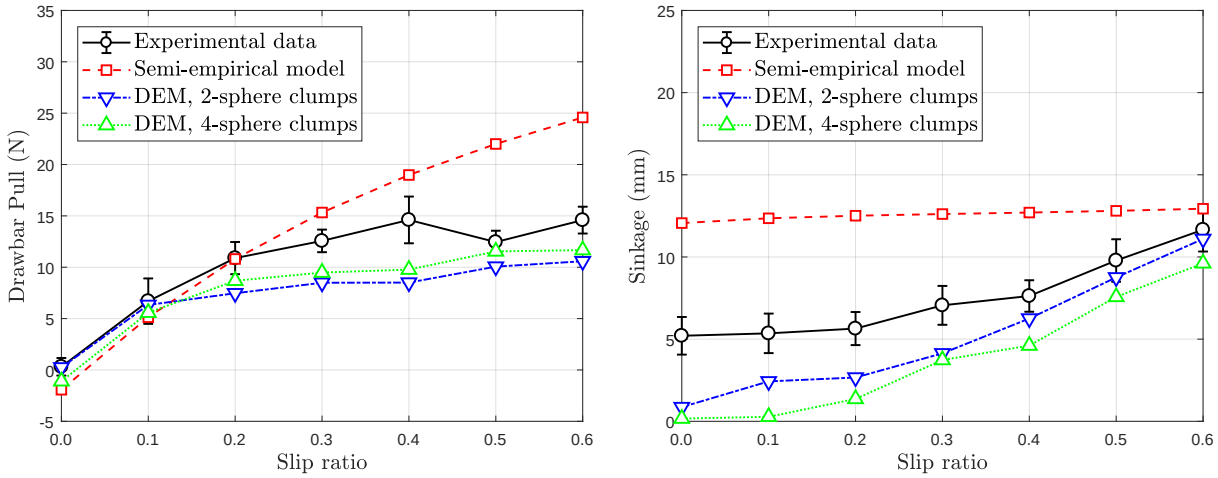

Figure 12: **Left**: Experimental drawbar pull, plotted as a function of the slip ratio, compared to the discrete element and semi-empirical results. **Right**: Experimental wheel sinkage, plotted as a function of the slip ratio, compared to the discrete element and semi-empirical results.

where only the energy contribution from the bending moment was taken into account. Let us take the quarter of the ellipse lying in the first quadrant and subdivide the x-axis, in the interval $[0,\, a]$, in $n \in \mathbb{N}$ points whose abscissa, x_i, is equal to $a\cos(t_i)$, where the parameter t_i represents equally space angles. The derivative of the ellipse for $y \geq 0$ is

$$\frac{dy}{dx} = -\frac{bx}{a^2\sqrt{1-\frac{x^2}{a^2}}},$$

thus the angle between the line tangent to the ellipse at $x = x_i$ and the x-axis can be determined. The difference between the angles formed with the x-axis by the two lines tangent to the ellipse at two successive points, i.e. x_i and x_{i+1}, gives the supplementary angle between two consecutive segments of the deformed shape. By subtracting the latter angle and the corresponding known angle in the undeformed configuration, the relative angle of rotation $\Delta\theta_{t_i}$ of the torsion spring is computed. Finally, by equating the expression of the strain energy of the continuum system given by Equation (5) with the total potential energy stored in the discretized system

$$\frac{W^2R^3}{EI}\left(\frac{\pi}{16}-\frac{1}{2\pi}\right) = 4\cdot\frac{1}{2}K_t\sum_{i=0}^{n}\Delta\theta_{t_i}^2,$$

the stiffness of the torsion springs is computed. The rim was discretized into 64 rigid parts and the rotational spring stiffness was evaluated equal to $170.38\,\mathrm{N\,mm\,deg^{-1}}$ and the stiffness of the radial springs was calculated equal to $4.98\,\mathrm{N\,mm^{-1}}$. In literature, Schäfer et al. (2010) applied a similar approach to simulate the elasticity of the ESA ExoMars rover wheel by subdividing the wheel into 24 rigid parts. This lumped parameter model was compared with the finite element model of the rim. A nonlinear analysis was performed with the Nastran solver (SOL106) with different values of the vertical load W: acceptable maximum relative error between 6.7% and 7.5% for the vertical displacement and maximum relative error between 6.7% and 6.8% for the horizontal displacement were computed. To validate the overall multibody model of the elastic wheel, an implicit nonlinear and static (SOL400) finite element model of the AMALIA wheel was developed. The finite element model consists of 9877 four-node iso-parametric flat plate elements (CQUAD4) and only 144 three-node elements used for mesh transition, for a total of 11422 grid points. The hub was modelled with a rigid body element (RBE2) and the ground as a single and fixed rigid body as illustrated in Figure 11 left. The hub vertical translation for the finite element and multibody models of the wheel are compared in Figure 11 right, which shows a minimum and maximum relative error of 1.7% and 8.9% respectively in the load range of interest.

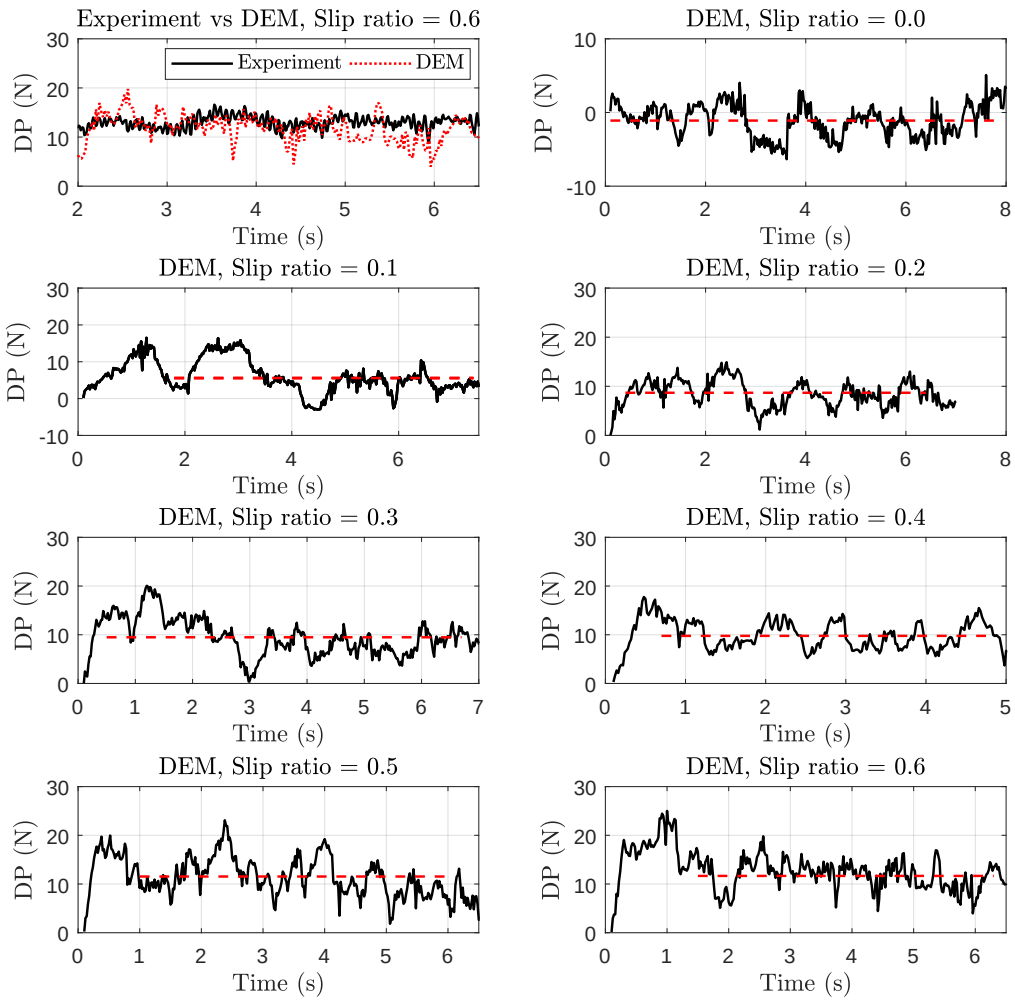

Figure 13: Drawbar pull time histories obtained from the multibody-discrete element co-simulations performed with the four-sphere clumps. The red dotted lines represent the drawbar pull average of the corresponding time series. In the top left graph the experimental and numerical drawbar pull time series for $s = 0.6$ are compared.

7 Results and discussion

Drawbar pull and sinkage of the AMALIA wheel obtained from both the discrete element simulations and the semi-empirical model are plotted as a function of the slip ratio in Figure 12 left and right respectively and compared with the laboratory tests.

Regarding the drawbar pull, both the classical and DEM models approximate well the experimental data especially for low slip values ($0.1 \div 0.3$). In particular for $s = 0.2$ the relative error between the classical terramechanics model and the experimental test is 0.77%, while the error for $s = 0.3$ increases to 21.99%. With the exception of $s = 0.0$, the discrete element simulations with four-sphere clumps perform better than the two-sphere clumps for the whole range of slip ratios considered, thanks to their more complex shape that increases the interlocking effect between the elements. For instance, the relative error for the four-sphere clumps in the case $s = 0.1$ is 1.48% and for the other clump type is 15.21%. For slip ratios in the range from 0.4 to 0.6, the parametric model predicts 18.99 N for the drawbar pull while the experimental test measures 13.24 N, hence with a relative error equal to 43.43%. This discrepancy may be explained

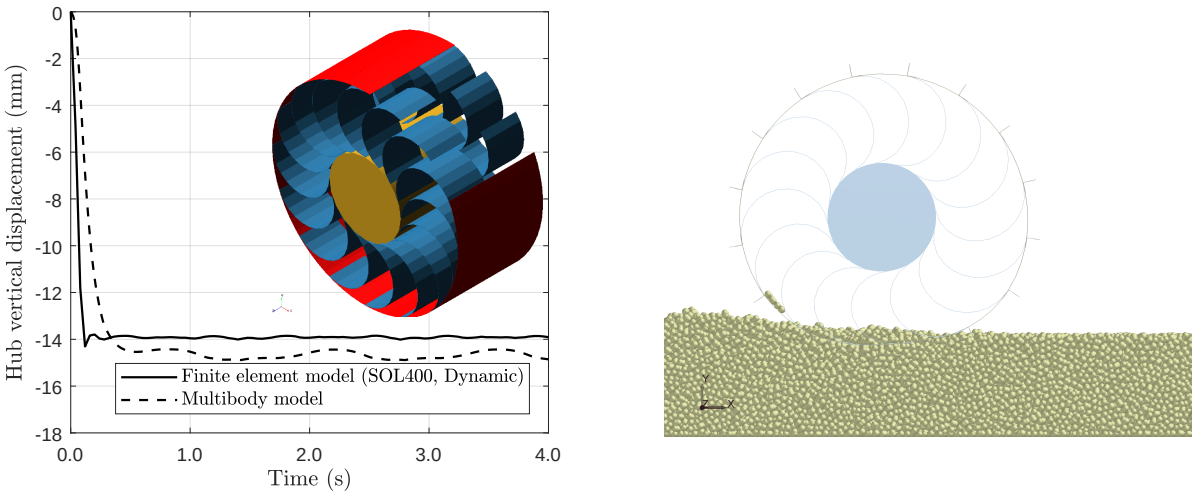

Figure 14: **Left**: Multibody simulation results of the flexible wheel rolling over a rigid surface compared to the finite element results of an implicit nonlinear dynamic analysis (SOL400) performed with the Nastran software. The rim segments of the multibody model are illustrated in red, while the two sets of semicircular beams are depicted in blue. **Right**: A longitudinal cross-section of a multibody-discrete element method co-simulation ($s = 0.6$) that highlights the deflection of the wheel and its interaction with the two-sphere clumps.

bearing in mind that the semi-empirical model results rely on some parameters, like the cohesive and friction moduli of deformation of the soil, taken from the literature. On the contrary, DEM models give acceptable predictions even for higher slip ratios. For example, by analyzing the four-sphere simulation results, for $s = 0.5$ the relative error is equal to 1.58% and for $s = 0.6$ the error reaches 15.1%. In Figure 13 the time histories of the drawbar pull for all the slip ratios are reported together with their averages used for plotting the graph in Figure 12; in addition, the experimental and DEM drawbar pull time series for $s = 0.6$ are compared. As previously said, because of the computational effort required by DEM tests, it was not possible to simulate, for example, a 80 s (i.e. $s = 0.6$) single wheel test, thus the experimental measures and numerical results for the sinkage were compared at $t = 7s$. In general, both parametric and DEM models performed better at high slip ratio ($s = 0.5$ and $s = 0.6$); for instance at $s = 0.6$ the two-sphere clump simulations give a 4.81% relative error. In this case the latter clump type performed better than the four-sphere particles because the simpler shape reduces the interlocking phenomenon. For low slips the accuracy decreased considerably, however these differences may be justified, as noted by Smith et al. (2013) by taking into account the inherent difficulties in measuring the sinkage of a wheel, especially a flexible one, in deformable soil. The latter researcher experienced an overestimation of the sinkage, probably because of the single sphere particles adopted, whereas in this study the sinkage of the flexible wheel is underestimated by the discrete element models.

8 Conclusions and future works

In this paper, the analysis of the tractive performance of a flexible wheel of a small planetary rover using the discrete element method was presented. Particular attention was devoted to understand how the particle shape might influence the simulation results. Despite the limited computational resources available, the DEM simulation results were in reasonable agreement with the experimental data. The most significant lesson learned from this activity is that a massive work is needed for the calibration of the DEM parameters; the tuning of the static friction coefficient, shear modulus and PD of the bulk material and the selection of the particle size and shape required to perform hundreds of direct shear and single wheel test co-simulations.

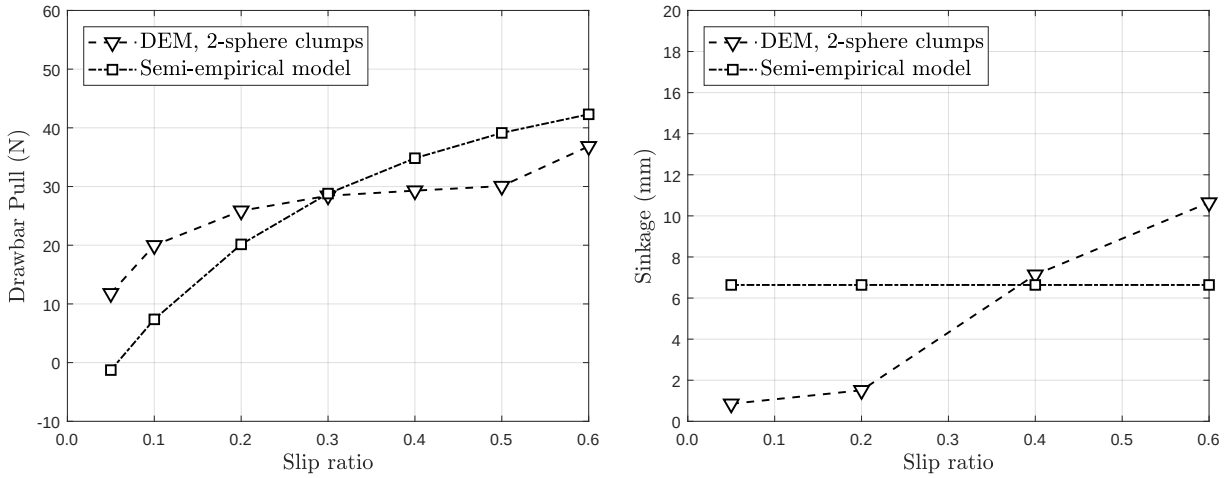

Figure 15: **Left**: Drawbar pull, as a function of the slip ratio, predicted by semi-empirical model and DEM simulations. **Right**: Sinkage, as a function of the slip ratio, predicted by semi-empirical model and DEM simulations.

The discrete element models developed are currently used for studying the performance of flexible wheels that in the future might replace the pneumatic tires of the T0-R0 rover, a six-wheeled vehicle built by Team DIANA, that was selected to compete at the upcoming European Rover Challenge[3] (September, 2018). In Figure 14 one of the flexible wheel concepts is shown. This wheel, whose radius and width are 130 mm and 120 mm respectively, features two sets of 16 semicircular beams, having radius equal to 40 mm and width of 50 mm, placed in radial direction. Both the rim and the beams are made of 0.3 mm thick steel sheets (AISI 304). The rim and each beam were discretized with 64 and 12 rigid bodies respectively; by using the procedure described in Section 6.2, the stiffness of the torsion springs constituting the rim and beams were computed equal to $85.63\,\mathrm{N\,mm\,deg^{-1}}$ and $47.61\,\mathrm{N\,mm\,deg^{-1}}$ respectively. The rolling of the wheel in contact with a rigid surface and subjected to a vertical load of 81.75 N was simulated both in the multibody and finite element environments; Figure 14 shows the good agreement of the multibody simulation results with respect to finite element ones of the hub vertical displacement during steady state (maximum and minimum relative errors of 6.21% and 3.88% respectively). A 670 mm long, 250 mm wide and 100 mm deep bin, with periodic boundaries in the x and z directions, was filled with two-sphere clumps; the packing density of the soil bin was set equal to 0.57. In Figure 15 the multibody-discrete element co-simulations of the drawbar pull and sinkage are compared to the semi-empirical simulation results. As in the AMALIA case, the semi-empirical model predicts higher values of the drawbar pull for wheel slips ranging from 0.3 to 0.6 (Figure 15 left) and higher wheel sinkage for low slips (Figure 15 right) with respect to the discrete element model; in this case, the values of the parameters c_1 and c_2 were restored to 0.4 and 0.15 respectively as suggested by Ishigami et al. (2011). A total of 14 co-simulations were run and the wall time taken by a 10 s virtual test with two-sphere clumps is about 1030 minutes.

Acknowledgments

The authors deeply thank: Gabriele Sandro Toro, responsible for the geotechnical laboratory at Università d'Annunzio (Pescara, Italy); the whole EDEM team and in particular Jennifer Currie and Julia Kokocinska; Daniele Catelani, Senior Project Manager at MSC Software; Team DIANA, space robotics group at Politecnico di Torino.

[3] http://roverchallenge.eu/2018/04/16/double-record-of-applications-for-the-european-rover-challenge-2018/

References

Bekker, M. G. (1956). Theory of land locomotion.

Bekker, M. G. (1960). Off-the-road locomotion. *Research and development in terramechanics*.

Bekker, M. G. (1969). Introduction to terrain-vehicle systems.

Briend, R. (2010). *Modelling Wheel-soil Interactions Using the Discrete Element Method for Tread Shape Optimization*. PhD thesis, McGill University Library.

Briend, R., Radziszewski, P., and Pasini, D. (2011). Virtual soil calibration for wheel–soil interaction simulations using the discrete-element method. *Canadian Aeronautics and Space Journal*, 57(1):59–64.

Coetzee, C. (2016). Calibration of the discrete element method and the effect of particle shape. *Powder Technology*, 297:50–70.

Coetzee, C. (2017). Calibration of the discrete element method. *Powder Technology*, 310:104–142.

Cundall, P. and Strack, O. (1979). A discrete numerical method for granular assemblies. *Geotechnique*, 29:47–65.

Das, N. (2007). *Modeling three-dimensional shape of sand grains using discrete element method.* PhD thesis, University of South Florida.

Derakhshani, S. M., Schott, D. L., and Lodewijks, G. (2015). Micro–macro properties of quartz sand: Experimental investigation and dem simulation. *Powder Technology*, 269:127–138.

EDEM (2017a). *EDEM 2017 User Guide: Creator*.

EDEM (2017b). *EDEM 2017 User Guide: Simulator*.

Favaedi, Y., Pechev, A., Scharringhausen, M., and Richter, L. (2011). Prediction of tractive response for flexible wheels with application to planetary rovers. *Journal of Terramechanics*, 48(3):199–213.

Genta, G. and Marenco, M. (2014). Design and testing of active suspensions for wheeled planetery rovers. In *65th International Astronautical Congress*, Toronto, Canada.

González-Montellano, C., Ayuga, F., and Ooi, J. (2011). Discrete element modelling of grain flow in a planar silo: influence of simulation parameters. *Granular Matter*, 13(2):149–158.

Ishigami, G., Otsuki, M., Kubota, T., and Iagnemma, K. (2011). Modeling of flexible and rigid wheels for exploration rover on rough terrain. In *the 28th International Symposium on Space Technology and Science, Okinawa, Japan, 5-12 JUne, 2011.*

Janosi, Z. and Hanamoto, B. (1961). The analytical determination of drawbar pull as a function of slip for tracked vehicle in deformable soils. In *In Proceedings of the 1st Int. Conf. on Terrain-Vehicle Systems, Torino, Italy.*

Johnson, J. B., Kulchitsky, A. V., Duvoy, P., Iagnemma, K., Senatore, C., Arvidson, R. E., and Moore, J. (2015). Discrete element method simulations of mars exploration rover wheel performance. *Journal of Terramechanics*, 62:31–40.

Knuth, M. A., Johnson, J., Hopkins, M., Sullivan, R., and Moore, J. (2012). Discrete element modeling of a mars exploration rover wheel in granular material. *Journal of Terramechanics*, 49(1):27–36.

Marigo, M. and Stitt, E. H. (2015). Discrete element method (dem) for industrial applications: Comments on calibration and validation for the modelling of cylindrical pellets. *KONA Powder and Particle Journal*, 32:236–252.

Matuttis, H.-G. and Chen, J. (2014). *Understanding the discrete element method: simulation of non-spherical particles for granular and multi-body systems.* John Wiley & Sons.

Nishiyama, K., Nakashima, H., Yoshida, T., Ono, T., Shimizu, H., Miyasaka, J., and Ohdoi, K. (2016). 2d fe–dem analysis of tractive performance of an elastic wheel for planetary rovers. *Journal of Terramechanics*, 64:23–35.

O'Sullivan, C. (2014). Advancing geomechanics using dem. In *Proc. International Symposium on Geomechanics from Micro to Macro*, volume 1, pages 21–32.

Pizette, P., Martin, C., Delette, G., Sornay, P., and Sans, F. (2010). Compaction of aggregated ceramic powders: From contact laws to fracture and yield surfaces. *Powder technology*, 198(2):240–250.

Schäfer, B., Gibbesch, A., Krenn, R., and Rebele, B. (2010). Planetary rover mobility simulation on soft and uneven terrain. *Vehicle System Dynamics*, 48(1):149–169.

Shmulevich, I. and Osetinsky, A. (2003). Traction performance of a pushed/pulled drive wheel. *Journal of Terramechanics*, 40(1):33–50.

Smith, W., Melanz, D., Senatore, C., Iagnemma, K., and Peng, H. (2013). Comparison of dem and traditional modeling methods for simulating steady-state wheel-terrain interaction for small vehicles. In *Proceedings of the 7th Americas Regional Conference of the ISTVS, Tampa, FL, USA*, pages 4–7.

Tsuji, Y., Tanaka, T., and Ishida, T. (1992). Lagrangian numerical simulation of plug flow of cohesionless particles in a horizontal pipe. *Powder technology*, 71(3):239–250.

Ucgul, M., Fielke, J. M., and Saunders, C. (2015). Three-dimensional discrete element modelling (dem) of tillage: Accounting for soil cohesion and adhesion. *Biosystems Engineering*, 129:298–306.

Wong, J.-Y. (1978). *Theory of ground vehicles*. John Wiley and Sons, Inc.

Wong, J.-Y. (1984). On the study of wheel-soil interaction. *Journal of Terramechanics*, 21(2):117–131.

Wong, J.-Y. (2010). *Terramechanics and off-road vehicle engineering: terrain behaviour, off-road vehicle performance and design*. Butterworth-heinemann.

Wong, J.-Y. and Reece, A. (1967a). Prediction of rigid wheel performance based on the analysis of soil-wheel stresses part i. performance of driven rigid wheels. *Journal of Terramechanics*, 4(1):81–98.

Wong, J.-Y. and Reece, A. (1967b). Prediction of rigid wheel performance based on the analysis of soil-wheel stresses: Part ii. performance of towed rigid wheels. *Journal of Terramechanics*, 4(2):7–25.

Young, W. C. and Budynas, R. G. (2002). *Roark's formulas for stress and strain*. McGraw-Hill.

Zhang, D. and Whiten, W. (1996). The calculation of contact forces between particles using spring and damping models. *Powder technology*, 88(1):59–64.

Zhu, H., Zhou, Z., Yang, R., and Yu, A. (2008). Discrete particle simulation of particulate systems: a review of major applications and findings. *Chemical Engineering Science*, 63(23):5728–5770.